Experimental and Theoretical Study of Bi$_2$O$_2$Se Under Compression

A. L. J. Pereira,*[†,‡] D. Santamaría-Pérez,[§] J. Ruiz-Fuertes,[§,∥] F. J. Manjón,*[†] V. P. Cuenca-Gotor,[†]
R. Vilaplana,[⊥] O. Gomis,[⊥] C. Popescu,[#] A. Muñoz,[○] P. Rodríguez-Hernández,[○] A. Segura,[§]
L. Gracia,[¶] A. Beltrán,[∇] P. Ruleova,[□] C. Drasar,[□] and J. A. Sans[†]

[†]Instituto de Diseño para la Fabricación y Producción Automatizada, MALTA Consolider Team, Universitat Politècnica de València, València 46022, Spain

[‡]Grupo de Pesquisa de Materiais Fotonicos e Energia Renovável - MaFER, Universidade Federal da Grande Dourados, Dourados, MS 79825-070, Brazil

[§]Departament de Física Aplicada — ICMUV, MALTA Consolider Team, Universitat de València, Burjassot 46100, Spain

[∥]DCITIMAC, MALTA Consolider Team, Universidad de Cantabria, Santander 39005, Spain

[⊥]Centro de Tecnologías Físicas, MALTA Consolider Team, Universitat Politècnica de València, València 46022, Spain

[#]CELLS-ALBA Synchrotron Light Facility, 08290 Cerdanyola, Barcelona, Spain

[○]Departamento de Física, Instituto de Materiales y Nanotecnología, MALTA Consolider Team, Universidad de La Laguna, Tenerife E38205, Spain

[¶]Departament de Química Física, MALTA Consolider Team, Universitat de València, Burjassot 46100, Spain

[∇]Departament de Química Física i Analítica, MALTA Consolider Team, Universitat Jaume I, Castellón 12071, Spain

[□]Faculty of Chemical Technology, University of Pardubice, Pardubice 532 10, Czech Republic

S *Supporting Information*

ABSTRACT: We report a joint experimental and theoretical study of the structural, vibrational, elastic, optical, and electronic properties of the layered high-mobility semiconductor Bi$_2$O$_2$Se at high pressure. A good agreement between experiments and *ab initio* calculations is observed for the equation of state, the pressure coefficients of the Raman-active modes and the bandgap of the material. In particular, a detailed description of the vibrational properties is provided. Unlike other Sillén-type compounds which undergo a tetragonal to collapsed tetragonal pressure-induced phase transition at relatively low pressures, Bi$_2$O$_2$Se shows a remarkable structural stability up to 30 GPa; however, our results indicate that this compound exhibits considerable electronic changes around 4 GPa, likely related to the progressive shortening and hardening of the long and weak Bi—Se bonds linking the Bi$_2$O$_2$ and Se atomic layers. Variations of the structural, vibrational, and electronic properties induced by these electronic changes are discussed.
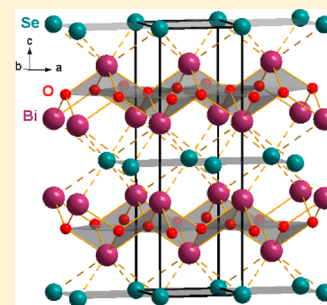
1. INTRODUCTION

In recent years, studies related to topological insulators (TIs) have attracted the attention of many research groups. TIs are a class of quantum materials in which time-reversal symmetry, relativistic effects, and an inverted band structure result in the occurrence, in an insulator bulk crystal, of electronic metallic states on the surface which are protected against nonmagnetic impurities or defects. Among such materials, layered compounds Bi$_2$Se$_3$, Bi$_2$Te$_3$, and Sb$_2$Te$_3$ were predicted and found to behave as TIs.[1−4] It must be stressed that TIs have promising applications in spintronic devices and dissipationless transistors based on the quantum spin Hall effect and quantum anomalous Hall effect,[5,6] as well the ability to host Majorana particles.[7] In fact, TIs have already found practical applications in advanced magnetoelectronic and optoelectronic devices.[8,9]

It has been recently suggested that there could be a close relationship between TIs and highly efficient thermoelectric materials (TMs);[10] therefore the search of new TIs is also important to find new TMs. In this context, the metal chalcogenide semiconductors belonging to the A$_2$X$_3$ (A = Sb, Bi; X = Se, Te) family with layered tetradymite structure have been of great interest mainly because of their exceptional thermoelectric (TE) properties, with Bi$_2$Te$_3$ and Sb$_2$Te$_3$ being the most widely used TMs at ambient conditions.[11,12]

The strong interest in improving the TE properties of TMs, especially in the most interesting temperature range for TE energy harvest (between 400 and 700 K), suggests to engineer the bandgap of the materials since the optimized TMs are predicted to be semiconductors with a bandgap $E_g = 10k_BT_{op}$, where k_B is the Boltzmann constant and T_{op} is the operating temperature of TE devices.[13] Additionally, there is a strong interest in increasing the chemical stability and in decreasing

the toxicity of chalcogenide-based TMs. All the above requirements are stimulating the study of layered compounds involving heavy elements such as Bi and Sb combined with O, S, and Se instead of Te. In this way, a decrease in toxicity and an increase of the chemical stability and of the bandgap will allow to reach the goal of achieving a figure of merit, ZT, near 3 in order to make a widespread use of TMs for TE energy harvest.[14]

Among the studied layered oxychalcogenides, Bi_2O_2Se has been found as a promising TM since it is an intrinsic n-type semiconductor with rather good TE properties around 800 K,[15] that can be enhanced under certain stresses, as predicted by *ab initio* calculations,[16] or by appropriate doping.[17,18] Most importantly, recent studies have shown that 2D nanometer-size thin films of Bi_2O_2Se exhibit an extraordinary high-mobility, which combined with its extraordinary chemical stability and large bandgap make this material a promising candidate for the realization of novel quantum phenomena, future logic devices, and flexible electronic applications.[19,20] In fact, the application of Bi_2O_2Se films in electronic applications has been recently proved.[21] Besides, it has been recently predicted that 2D bismuth oxychalcogenides are exceptional ferroelastic/ferroelectric materials with interest in a number of applications still to be developed.[22]

At room pressure, Bi_2O_2Se crystallizes in a layered body-centered tetragonal structure (space group No. 139, $I4/mmm-D_{4h}$[17]). In this structure, Se, O, and Bi atoms are located at $2a$ $(0,0,0)$, $4d$ $(0,1/2,1/4)$, and $4e$ $(0,0,z)$ Wyckoff sites, respectively. Therefore, the z coordinate of the Bi atom is the only free atomic coordinate in the structure. In this structure (Figure 1(top)), Bi and O atoms form Bi_2O_2 layers perpendicular to the [001] direction where Bi and O atoms are 4-fold coordinated and form a square pyramid with Bi–O bond lengths of 2.3 Å. On the other hand, Se atoms form atomic layers located between the Bi_2O_2 layers. A weak link between Bi_2O_2 and Se atomic layers occurs thanks to weak Bi–Se electrostatic interactions (each Bi atom forms four Bi–Se bonds so that each Se is 8-fold coordinated) with a length above 3.0 Å. In summary, the Bi_2O_2Se structure can be understood as a layered structure where Bi_2O_2 layers and Se atomic layers are 3D linked thanks to weak Bi–Se electrostatic interactions and where the lone electron pair (LEP) of each Bi atom is directed perpendicularly to the layers toward the center of the four Se atoms interacting with each Bi atom. In fact, since the closest Bi atoms of different layers are aligned along the c axis, their corresponding LEPs are facing to each other across the Se atomic layer.

A way of interpreting the structure of the Bi_2O_2 sublattice is by applying the inverse Zintl–Klemm concept;[23,24] i.e., a "Zintl polycation" $(Bi_2O_2)^{2+}$ is formed when the two electropositive Bi atoms formally transfer 2 electrons to the Se atom. In this way, each Bi atom becomes a pseudo Ψ-Pb atom and the Bi_2O_2 sublattice adopts the same layered structure as litharge PbO (Pb_2O_2 and $(Bi_2O_2)^{2+}$ are isoelectronic).[25] This view is consistent with previous reports where Bi_2O_2 layers are assumed to be insulating and conductivity of Bi_2O_2Se is mainly due to the large conductivity along the Se layers.[19,20] It must be stressed that the formation of layered compounds seems to be a common feature in many Sb- and Bi-related sesquioxides and sesquichalcogenides, like the polymorphs α-Bi_2O_3, β-Bi_2O_3, HPC-Bi_2O_3, Sb_2S_3, Bi_2S_3, Bi_2Se_3, Sb_2Te_3, and Bi_2Te_3,[26–30] and also in other related compounds, like BiSe, BiTe, and Bi_4Te_3.[31]
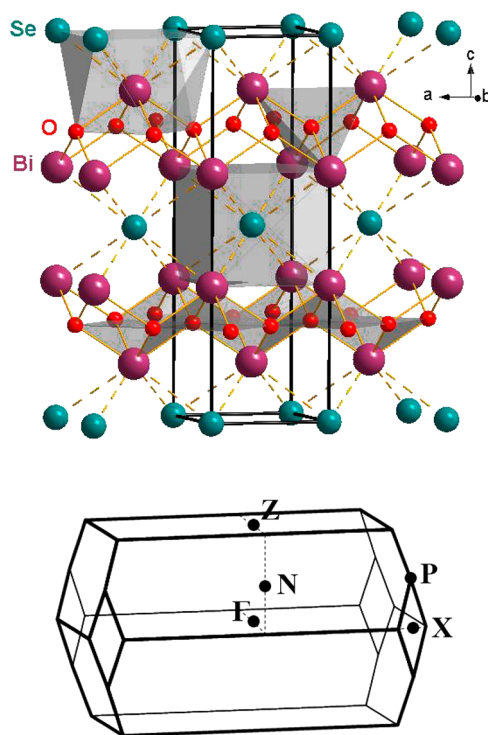

Figure 1. (Top) Crystalline structure of tetragonal Bi_2O_2Se at 1 atm. Large magenta balls represent Bi atoms, while small red balls represent O atoms and medium-sized green balls represent Se atoms. Bi atoms are linked to four O atoms with short bonds (solid lines) and to four Se atoms with long bonds (dashed lines). O atoms are surrounded by four Bi atoms and Se atoms are surrounded by eight Bi atoms. The structure is composed by alternate Bi_2O_2 layers, where Bi atoms show 4-fold coordination, and atomic Se layers. (Bottom) Brillouin zone of the body-centered tetragonal unit cell with $c/a > 1$.

Pressure is a thermodynamic magnitude and a powerful tool to unravel the intrinsic properties of materials because it is cleaner than chemical doping and simpler to analyze than temperature. Therefore, the understanding of the behavior of Bi_2O_2Se under compression will help to improve and fully exploit the great potential of the electronic and TE properties of this interesting material. Despite of the increasing interest in bismuth oxychalcogenides, most of the properties of layered Bi_2O_2Se are barely known specially at high pressures (HPs). In this respect, it must be noted that layered compounds of the Bi_2Se_3 family studied at HP have exhibited novel phenomena such as structural phase transitions at low pressures, pressure-induced electronic topological transition (ETT) or Lifshitz transition, and pressure-induced superconductivity.[26] Furthermore, HP exploration of Sillén-type compounds, which are isostructural to Bi_2O_2Se, like iron-based pnictide super-conductors, have shown changes in the Fermi surface topology and new superconductor phases usually related to a tetragonal to collapsed tetragonal pressure-induced phase transition at relatively low pressures.[32–38]

In this work, we report a joint experimental and theoretical HP study of the structural, vibrational, elastic, optical, and electronic properties of Bi_2O_2Se up to 30 GPa. No other study of Bi_2O_2Se under compression has been previously reported to our knowledge. For that purpose, X-ray diffraction (XRD), Raman scattering (RS) and optical absorption measurements have been combined with *ab initio* total-energy structural and lattice-dynamics calculations. It has been found that, unlike

other isostructural Sillén-type compounds,[32−38] the tetragonal structure of Bi_2O_2Se presents a remarkable high stability with no phase transition up to 30 GPa. Furthermore, HP studies of both end members Bi_2O_3 and Bi_2Se_3 show phase transitions below 30 GPa.[27−29,39]

Curiously enough, interesting electronic changes in Bi_2O_2Se occur near 4 GPa consisting of crossing and anticrossing behaviors of the topmost and second topmost valence bands at different points of the Brillouin zone. These changes are likely related to the progressive shortening and hardening of the long and weak Bi−Se bonds between the layers. Therefore, this study will help to understand the behavior of Bi_2O_2Se and other Sillén-type compounds under compression and, in general, those of layered materials lacking van der Waals forces between their layers.

2. EXPERIMENTAL METHOD

Bi_2O_2Se polycrystalline material was recently synthesized from Bi_2Se_3 and Bi_2O_3 by solid state reaction in an evacuated quartz ampoule.[40] In accordance with the literature, it was observed that the prepared samples crystallize in the space group 139, $I4/mmm−D_{4h}$,[17] with lattice parameters $a = 3.8859$ Å and $c = 12.2055$ Å and yield a unit-cell volume $V_0 = 184.30$ Å^3. The z atomic positions of Bi and O are $z(Bi) = 0.355(1)$ and $z(O) = 0.250(3)$. All these parameters compare well within 0.2% with structural of the ICSD-2903 entry.[41] This structure is the same as that of Nd_2O_2Te[42] and the recently synthesized Bi_2O_2Te[43] and it is composed of insulating $Bi_2O_2^{2+}$ layers separated by conducting square $Se^{2−}$ atomic layers (Figure 1(top)). Structural analyses have shown no spurious phases or other phases related to Bi, O, or Se. On the other hand, energy-dispersive X-ray spectroscopy (EDS) analyses showed that the composition of the sample is not purely stoichiometric and has a slight excess of O and a slight deficiency of Se with respect to Bi with an approximate stoichiometry of $Bi_2O_{2.2}Se_{0.8}$.

Both powder angle-dispersive XRD measurements at room and HP (up 22 GPa) were performed at room temperature in an Xcalibur diffractometer with the lines $K\alpha_1$ and $K\alpha_2$ of a molybdenum source ($\lambda = 0.7093$ and 0.7136 Å, respectively) with a Merrill−Bassett-type diamond anvil cell (DAC) with diamond culets of 400 μm in diameter.[44] Pressure was determined by the luminescence of small ruby chips evenly distributed in the pressure chamber with an error below 0.2 GPa in the whole pressure range studied.[45] A more accurate powder angle-dispersive XRD experiment was also performed up to 21 GPa at room temperature in the BL04-MSPD beamline at ALBA synchrotron facility.[46] This beamline is equipped with Kirkpatrick-Baez mirrors to focus the monochromatic beam and a Rayonix CCD detector with a 165 mm diameter active area and was operated with a wavelength of 0.4246 Å. Cu powder was used as the internal pressure gauge using the values $V_0 = 47.24$ Å^3, $B_0 = 133$ GPa and $B_0' = 5.01$, corresponding to a third-order Vinet equation of state (EOS) which gives a pressure error below 1% in the 0−20 GPa range.[47] Integration of 2D diffraction images was performed with Dioptas software[48] while structural analysis was performed by Le Bail refinements to the XRD patterns recorded at all pressures with Fullprof[49] and PowderCell[50] program packages.

Unpolarized HP-RS measurements up to 28.3 GPa were carried out with a Horiba Jobin Yvon LabRAM HR microspectrometer equipped with a thermoelectrically cooled multichannel charge-coupled device detector which allows a spectral resolution better than 2 cm$^{−1}$. The signal was collected in backscattering geometry exciting with a HeNe laser (632.8 nm line) with a power of less than 10 mW. The measurements were performed at three different zones with different types of filters to ensure that the sample was not burned during laser excitation. Nonetheless, it was not observed any significant difference in the spectrum apart from a change in the intensity of the peaks. Pressure was also determined by the ruby luminescence method.[44] Phonons were analyzed by fitting Raman peaks with a Voigt profile fixing the Gaussian line width (1.6 cm$^{−1}$) to the experimental setup resolution.

Finally, HP optical absorption measurements at room temperature up to 19.8 GPa were performed in a plate of Bi_2O_2Se 3-μm-thick and 100×100 μm^2 in size uniformly cleaved along the (001) plane of a single crystal. Therefore, our optical absorption measurements were performed with the electric field geometry $E \perp c$. HP optical absorption measurements were performed in a membrane-type DAC with 500 μm diameter diamond culet anvils and using ruby chips for pressure calibration. The pressure chamber was a hole of 250 μm in diameter made on an Inconel gasket preindented to 45 μm in thickness. HP optical absorption experiments at room temperature were performed by the sample-in−sample-out method using a micro-optical system[51,52] composed of a halogen lamp, one CaF_2 lens, two Cassegrain objectives, and two spectrometers in the UV−vis and vis−NIR range, respectively. It must be stressed that all HP measurements were performed with a 16:3:1 methanol−ethanol−water mixture as a pressure-transmitting medium that provides hydrostatic conditions up to 10 GPa and quasi-hydrostatic conditions up to the maximum pressure attained in our experiments.[53] Possible effects of nonpurely hydrostatic conditions have been described elsewhere.[54]

3. COMPUTATIONAL DETAILS

Ab initio total-energy calculations were performed within the framework of density functional theory (DFT)[55] to study the structural, vibrational, elastic, optical and electronic properties of Bi_2O_2Se under pressure. The Vienna *ab initio* simulation package (VASP)[56] was used to carry out simulations with the projector augmented wave (PAW)[57] pseudopotentials. The PAW scheme replaces core electrons and makes smoothed pseudovalence wave functions taking into account the full nodal character of the all-electron charge density in the core region. The set of plane waves employed was extended up to a kinetic energy cutoff of 520 eV due to the presence of oxygen in the compound under study. The generalized gradient approximation (GGA) was used for the description of the exchange-correlation energy within the PBEsol prescription.[58] The Brillouin zone (BZ) of this body-centered tetragonal structure (with $c > a$) was sampled with a dense Monkhorst−Pack grid of special k-points.[59] With the cutoff energy and the k-point sampling employed, a high convergence of 1−2 meV per formula unit in the total energy is achieved. This ensures an accurate calculation of the forces on atoms. At a set of selected volumes, the structure was fully relaxed to the optimized configuration through the calculation of the forces on atoms and the stress tensor until the forces on the atoms were smaller than 0.005 eV/Å and the deviations of the stress tensor from a diagonal hydrostatic form were lower than 0.1 GPa.

The optimized structure at different pressures was used to study the electronic properties of Bi_2O_2Se taking into account the spin orbit coupling (SOC). The band structure was analyzed along the high-symmetry directions of the BZ. We

want to emphasize that the BZ of Bi_2O_2Se is that of Sillén-type compounds, like $SrFe_2As_2$;[38] i.e., that corresponding to a body-centered tetragonal structure (Figure 1(bottom)) and not the simple tetragonal BZ recently used in several calculations of Bi_2O_2Se.[19,22,60,61] The path suggested for this structure (space group 139, $I4/mmm$ with $c > a$) by Bradly and Cracknell and used at the Bilbao server web page was used to plot the electronic band structure and phonon dispersion curves (PDCs).[62,63]

Lattice-dynamics calculations were performed to study the phonons at the Γ point of the BZ using the direct force constant approach (or supercell method). The diagonalization of the dynamical matrix provides the frequency and symmetry of the phonon modes. To obtain the PDCs, along high-symmetry directions of the BZ, and the one-phonon density of states (PDOS), similar calculations were performed using appropriate supercells, which allow the PDCs at k-points to be obtained commensurate with the supercell size.[64] Finally, in order to study the HP mechanical stability of Bi_2O_2Se, the elastic stiffness constants were determined employing the stress theorem.[65] The optimized structures were strained, at different pressures, taking into account their symmetry.[66]

4. RESULTS

4.1. Structural Properties under Pressure. Angle-dispersive XRD patterns of Bi_2O_2Se with increasing pressure up to 22 GPa are shown in Figure 2. Le Bail refinements to the XRD patterns recorded at all pressures were performed using the tetragonal $I4/mmm$ structure of Bi_2O_2Se (see structural data of synchrotron radiation measurements in Table S1 in the

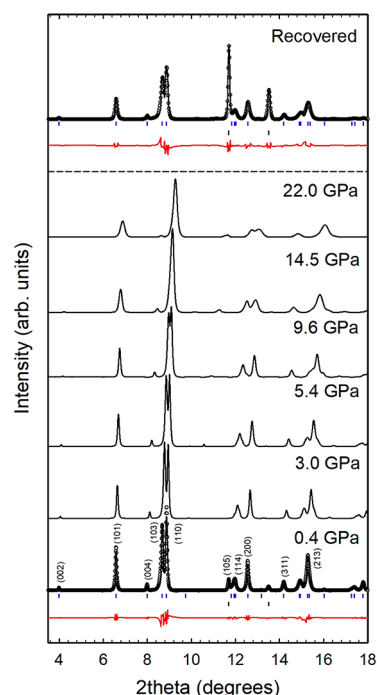**Figure 2.** Angle-dispersive XRD patterns of Bi_2O_2Se measured at different pressures up to 22 GPa at room temperature and on decreasing pressure to room pressure (top pattern). The low-pressure patterns (in circles) include the calculated LeBail (black line) and difference (red line) XRD profiles. Blue and black vertical markers indicate the Bragg reflections of the tetragonal Bi_2O_2Se phase and the Cu pressure gauge, respectively.

Supporting Information). These values at 300 K are in agreement with our *ab initio* calculations at 0 K that underestimate the experimental volume by only 0.5%; i.e., well within the error margin of calculations. Noteworthy, our experimental and theoretical values are also in good agreement with those previously found in the literature.[15]

All diffraction peaks shift to larger angles on increasing pressure up to 22 GPa. This result is coherent with the decrease of interplanar distances at HP. No additional diffraction lines or abrupt intensity changes were observed, thus indicating the absence of a structural phase transition. Upon compression, only two interesting phenomena can be noted: (i) the overlap of intense peaks related to the (103) and (110) planes above 14.5 GPa and (ii) the appearance of a low-intensity peak at $\sim11°$ above 3.0 GPa (Figure 2). This peak presents a large shift to high angles at HP, remains up to the maximum pressure of our study and is not related to the Bi_2O_2Se structure. In order to find the origin of this peak, we tried to refine the HP-XRD patterns using some possible structures related to elemental Bi, O and Se. In this way, this peak was tentatively assigned to the most intense reflections of the $\beta-O_2$ and $\varepsilon-O_2$ phases below and above 10 GPa, respectively.[67,68] The high compressibility of these solid phases of oxygen would explain the large shift rate to higher angles observed in the measurements and is consistent with the excess of O found by EDS in original samples. Despite this fact, HP-XRD patterns mainly correspond to the initial tetragonal Bi_2O_2Se phase up to 22 GPa, indicating that Bi_2O_2Se does not present any clear phase transition. On pressure downstroke, the diffraction pattern obtained after opening the cell is identical to that of the initial sample (see top of Figure 2). The lack of observation of reflections related to oxygen near room pressure on upstroke and downstroke is consistent with our hypothesis since oxygen is liquid near room conditions and no reflections from a solid phase are expected to be seen.

The pressure dependence of the experimental and theoretical lattice parameters a and c of Bi_2O_2Se is shown in Figure 3(left). The axial compressibility, defined as $\kappa_x = -\frac{1}{x}\frac{\partial x}{\partial P}$ ($x = a, c$), obtained from a Birch–Murnaghan (BM) EOS fit of the experimental data[69] is reported in Table 1 and is in good agreement with our theoretical results. Deviations of experimental lattice parameters and unit cell volume above 10 GPa with respect to theoretical estimates are likely caused by nonhydrostatic stresses in the sample caused by the loss of hydrostatic conditions of the pressure-transmitting medium.[53] As expected for a 2D compound, the c-axis compressibility is much larger than the a-axis compressibility. Moreover, the c/a ratio (inset of Figure 3(left)) was found to decrease smoothly with pressure in good agreement with our calculations, as it is usual in many layered materials. However, the compressibility of the c axis (6.4×10^{-3} GPa^{-1}) is much smaller than in other layered materials with van der Waals forces between the layers, like Bi_2Se_3 (38.5×10^{-3} GPa^{-1}).[39] This result is consistent with the larger strength of weak electrostatic interlayer Bi–Se interactions than of interlayer van der Waals forces. For completeness, the theoretical evolution of the z coordinate of Bi at HP is given at the inset of Figure 3(right). It can be observed that no clear change of the theoretical c/a ratio or of the z coordinate of Bi is observed in the range up to 40 GPa that could indicate a second-order pressure-induced phase transition from a tetragonal to a collapsed tetragonal structure, unlike in other Sillén-type compounds.[32−38]
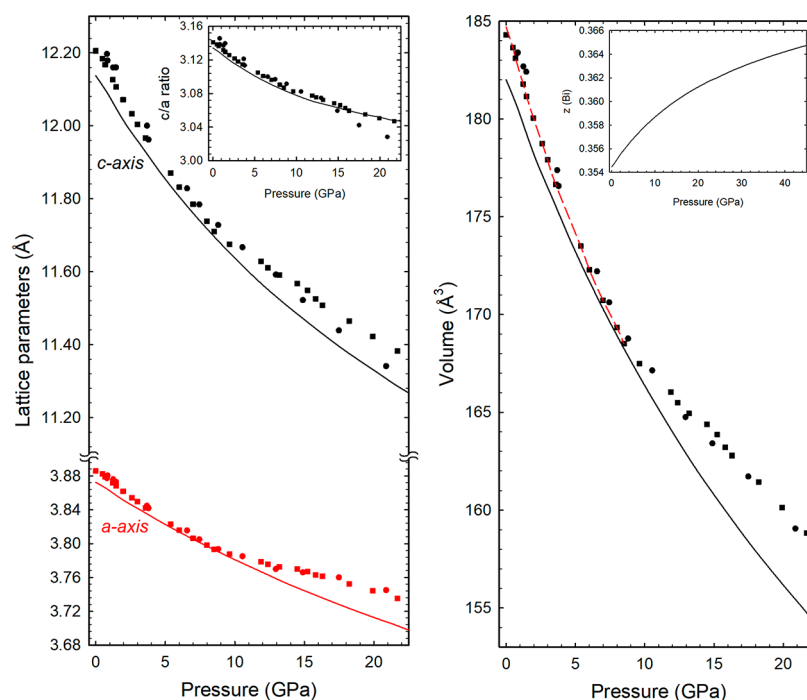
Figure 3. Experimental (symbols) and theoretical (lines) pressure dependence of the lattice parameters a and c (left) and of the unit-cell volume (right) for Bi_2O_2Se. Insets show the pressure dependence of the c/a ratio (left) and the z(Bi) coordinate (right). Experimental data include those from our in-home Xcalibur diffractometer (squares) and from the ALBA-CELLS beamline (circles). Errors in the determination of parameters are indicated by symbol sizes. In the volume plot, the solid black line is the EOS fit to the theoretical data while the dashed red line is the EOS fit to experimental data in the quasi-hydrostatic pressure range.

Table 1. EOS Parameters and Axial Compressibilities of Bi_2O_2Se at Room Pressure

	V_0 (Å³)	B_0 (GPa)	B_0'	κ_a (10^{-3} GPa⁻¹)	κ_c (10^{-3} GPa⁻¹)
experimental	184.69(8)	71.5(13)	5.6(3)	3.6(2)	6.4(2)
theoretical	183.8	88.17	4.86	3.0	5.9

Figure 3(right) shows the experimental and theoretical pressure dependence of the unit-cell volume of Bi_2O_2Se up to 22 GPa. A third-order BM EOS was used to fit our $P-V$ data to obtain the zero pressure volume, V_0, bulk modulus, B_0, and its pressure derivative, B_0', in the quasi-hydrostatic pressure range of the pressure transmitting medium (0−10 GPa). Experimental and theoretical data are summarized in Table 1 showing rather good agreement up to 22 GPa, thus the presence of any first-order phase transition can be clearly excluded. It can be stressed that the experimental compressibility of tetragonal Bi_2O_2Se is found between that of its constituent materials, α-Bi_2O_3 (B_0 = 85.4 GPa[28]) and layered Bi_2Se_3 (B_0 = 53 GPa[39]). It is noteworthy that the bulk modulus of Bi_2O_2Se is larger than that of other sesquioxides with channel-type structure, like β-Bi_2O_3 (B_0 = 34 GPa[29]), and larger than that of layered sesquichalcogenides, like Bi_2Se_3, Sb_2Te_3 (B_0 = 40 GPa[70]), and Bi_2Te_3 (B_0 = 40.9 GPa[71]). These results can be understood by considering that Bi_2O_2Se is a layered material where Bi_2O_2 layers are separated by Se square arrays showing weak Bi−Se electrostatic interactions at room pressure instead of a standard van der Waals gap between Bi_2O_2 layers. As already commented, since the van der Waals gap is much more compressible at low pressures than weak electrostatic interactions, Bi_2O_2Se shows a smaller compressibility (larger bulk modulus) at room pressure than usual layered compounds with van der Waals gap, like those of the Bi_2Se_3 family.

The good agreement between experimental and theoretical data allows us to exploit theoretical data where experimental data are lacking, since no reliable Rietveld refinement of XRD patterns could be performed (due to texturing effects of the polycrystalline sample) to obtain experimental atomic parameters and bond distances. Figure 4 presents the pressure dependence of the theoretical Bi−O, Bi−Se, Se−O, and interlayer Bi−Bi distances as well as of the Bi_2O_2 layer thickness. As can be observed, the Bi−O bond distance is much smaller than the Bi−Se distance at room pressure, thus indicating the strong ionic−covalent character of the Bi−O bonds and the weak electrostatic character of the Bi−Se bonds. This result justifies the 4-fold coordination of Bi and the 2D character of Bi_2O_2Se at room pressure and its easy exfoliation. Regarding the pressure dependence of the bond distances, it can be observed that they decrease with increasing pressure in a monotonous way. Notably, while the Bi−O bond distance decreases at a rate of -4.3×10^{-3} Å/GPa at room pressure, the Bi−Se bond distance decreases more than three times faster (-14.8×10^{-3} Å/GPa). This strong decrease of the Bi−Se distance also correlates with the strong decrease of the Bi_2O_2 interlayer distance (-29.5×10^{-3} Å/GPa) given by the interlayer Bi−Bi distance which results in a strong decrease of the c axis (-78.1×10^{-3} Å/GPa). The strong decrease of the interlayer distance with pressure contrasts with the negligible decrease of the layer thickness with pressure (-0.2×10^{-3} Å/GPa), which in turn is related to the small increase of the Bi z
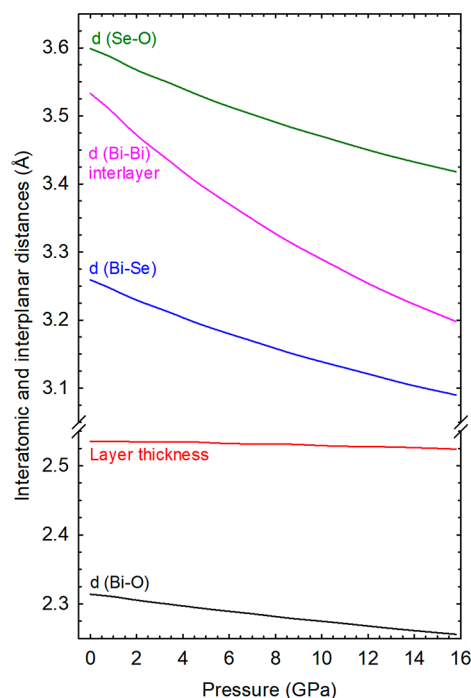
Figure 4. Pressure dependence of the theoretical interatomic and interplanar distances in Bi_2O_2Se.

coordinate. Note that the Bi_2O_2 layer thickness decreases at a smaller rate than the Bi–O bond distance, thus pointing to a decrease of the Bi–O–Bi angle inside the layer with pressure. For comparison with other Sillén-type compounds, the structural values found in Bi_2O_2Se are between those found for $SrRh_2P_2$ and $BaRh_2P_2$ since the interlayer Bi–Bi distance (z coordinate of Bi) at room pressure is 3.59 Å (0.354) and those for the P–P distance (z coordinate of P) in $SrRh_2P_2$ and $BaRh_2P_2$ are 3.284 Å (0.36) and 3.737 Å (0.351), respectively.[32] In these two compounds, the rate of decrease of the interlayer P–P distance (equivalent to Bi–Bi distance in Bi_2O_2Se) is of -23×10^{-3} Å/GPa which is smaller than in Bi_2O_2Se. A considerable decrease of the interlayer P–P distance occurs in $SrRh_2P_2$ around 6 GPa from a nonbonding to a bonding state, which does not occur in $BaRh_2P_2$ at least up to 11 GPa; however, a phase transition at higher pressure (likely around 20 GPa) is expected when the P–P distance decreases below 3.1 Å.[32] Such bondings are typical of light elements (O, S, N, P, and As), but not of heavy elements, like Bi, so a collapse of the tetragonal structure, like in $SrRh_2P_2$, $BaRh_2P_2$, $LaCo_2P_2$, $EuCo_2P_2$, $EuFe_2P_2$, and $EuRu_2P_2$,[32,33] is not expected to occur in Bi_2O_2Se. It remains to be seen what happens in Sb-based Sillén-type compounds.[34]

It must be stressed that despite the strong decrease of the Bi–Se distance, the value of this distance does not decrease below 3.0 Å even up to 30 GPa, therefore, despite the Bi–Se bond length decreases and its strength hardens at HP, Bi maintains its 4-fold coordination. Therefore, Bi_2O_2 layers are almost unaffected by pressure and the effect of pressure is a progressive and slight contraction of the Bi_2O_2 interlayer thickness. In this way, we can affirm that Bi_2O_2Se still behaves as a 2D material at HP even beyond 30 GPa since there is no net increase of Bi coordination between room pressure and 30 GPa. The progressive and monotonous compression of the interlayer distance contrasts with observations in van der Waals-based 2D materials, where the strong compression of the

interlayer distance at low pressures is followed by a hardening of the interlayer van der Waals interactions and then results in a considerable decrease of the layer thickness at low pressure and an almost negligible decrease of the layer thickness above certain pressure. Thus, all our results on the HP behavior of Bi_2O_2Se are clearly related to the lack of a van der Waals gap between the layers and the presence of a weak electrostatic Bi–Se interaction between the layers in 2D Bi_2O_2Se.

4.2. Vibrational Properties under Pressure. As regards the lattice dynamics of Bi_2O_2Se, group theoretical considerations of the Bi_2O_2Se structure in the *I4/mmm* space group indicates that there are 10 normal modes of vibration at Γ whose mechanical decomposition is[72]

$$\Gamma = 1A_{1g}(R) + 2A_{2u}(IR) + 1B_{1g}(R) + 2E_u(IR)$$
$$+ 2E_g(R) + A_{2u} + E_u$$

where A_{1g}, B_{1g} and E_g modes are Raman-active (R) and A_{2u} and E_u are infrared-active (IR). Therefore, there are four Raman-active modes ($\Gamma_{Raman} = A_{1g} + B_{1g} + 2E_g$), four infrared-active (IR) modes ($\Gamma_{IR} = 2A_{2u} + 2E_u$), and two acoustic modes ($\Gamma_{Acoustic} = A_{2u} + E_u$). Note that E modes are doubly degenerated. Table 2 summarizes the frequencies of the

Table 2. Experimental and Theoretical Raman (R) and Infrared (IR) Mode Frequencies of Bi_2O_2Se at Room Pressure

symmetry	exp freq (cm^{-1})	theor freq (cm^{-1})	assignment
E_u (IR)		59.2	Bi and Se out-of-phase movement along the layer (shear interlayer mode)
A_{2u} (IR)		64.5	Bi and Se out of-phase movement perpendicular to the layer (longitudinal interlayer mode)
E_g (R)		72.0	Bi out-of-phase interlayer movement along the layer
A_{1g} (R)	159.2	165.7	Bi out-phase interlayer movement perpendicular to the layers (breathing mode of the layers)
E_u (IR)		293.9	O in-phase intralayer movement along the layer
B_g (R)		369.4	O out-of-phase intralayer movement perpendicular to the layer
A_{2u} (IR)		402.8	O in-phase intralayer movement perpendicular to the layer
E_g (R)		444.0	O out-of-phase intralayer movement along the layer

experimental and theoretical vibrational modes at Γ in Bi_2O_2Se at room pressure together with the assignment of the vibrational modes to atomic movements thanks to the program J-ICE.[73] A description of vibrational modes and its comparison with other layered materials is provided in the Supporting Information.

RS measurements in Bi_2O_2Se at selected pressures up to 28 GPa (Figure 5(left)) show that the most intense Raman peak at room pressure is observed around 159 cm^{-1} and, according to theoretical calculations, would correspond to the A_{1g} mode (Figure 5(right)). The E_g mode, theoretically predicted at 72.0 cm^{-1} at room pressure, is not experimentally observed at room pressure because it is in the limit of detection of our system and in a very noisy region of the RS spectrum; however, this peak is clearly seen above 3.8 GPa. It must be noted that our RS spectrum at room pressure is similar to that previously reported
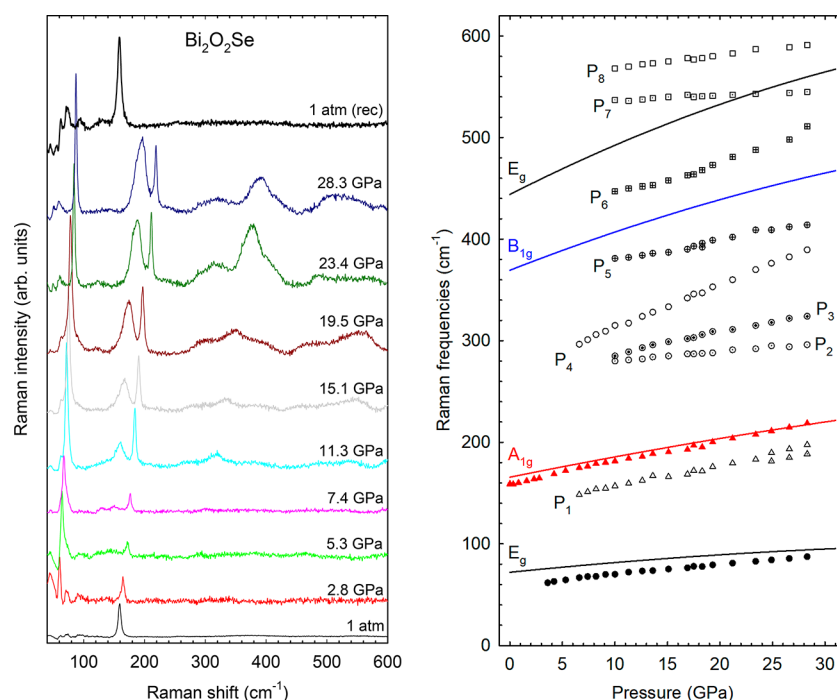
Figure 5. (Left) Room-temperature Raman spectra of Bi_2O_2Se at selected pressures up to 28.3 GPa. The top spectrum corresponds to the recovered sample after decompression. (Right) Experimental (symbols) and theoretical (lines) pressure dependence of the Raman-active modes of Bi_2O_2Se. Different colors represent Raman-active modes of different symmetries.

for bulk samples.[20] As regards the high-frequency B_{1g} and E_g modes at room pressure, they are theoretically predicted at 369.4 and 444.0 cm^{-1}, respectively; however they were not observed in our RS spectrum neither it was in previous measurements.[20] Only a broad band near 350 cm^{-1} is observed which is close to the position expected for the B_{1g} mode.

At present we have no explanation for the non-observation of the high-frequency Raman-active modes of Bi_2O_2Se even at room pressure. It could be due to their intrinsically small Raman scattering cross-section (RS measurements with very long exposure time and/or with high laser intensity were also performed) or to phonon damping of longitudinal optic (LO) phonons caused by the large carrier concentration in this n-type semiconductor. In this context, it could be possible that the weak broad bands observed in the high-frequency region could likely be due to plasmon-phonon coupling L^+ or L^- bands of the B_{1g} and E_g modes, as it occurs in many highly doped semiconductors.[74,75] A further study is needed to verify this hypothesis. It is well-known that plasmon-phonon coupling severely limits the mobility of carriers,[76] so this coupling could explain the rather low mobility ($\sim$150 cm^2/(V s)) found in bulk Bi_2O_2Se at room temperature in comparison to low temperature where carriers are freezed.[19] Additional proofs have to be made in order to resolve this controversy. In case that phonon-plasmon coupling was responsible for the non-observation of high-frequency Raman modes, we propose that observation of high-frequency B_{1g} and E_g Raman-active modes at room pressure could be a good test to monitor the synthesis of Bi_2O_2Se samples with low carrier concentration in order to improve the mobility of carriers at room temperature.

Since RS spectra of Bi_2O_2Se up to 28.3 GPa were taken with the same power and exposure time and in the same zone of the sample, we can reasonably compare the absolute intensity of different peaks. In particular, the intensity of the A_{1g} mode decreases from 0.3 to 4.2 GPa and increases above this pressure

with increasing pressure. This change of intensity is likely related to a change of the electronic polarizability due to changes of electronic origin as will be commented in the next section since they cannot be ascribed to structural changes related to the Bi LEP, unlike in other Bi-related compounds as β-Bi_2O_3.[29,77] Additionally, an increase in the intensity of Raman peaks, followed by the rise of new broad bands (mainly at 154.7 cm^{-1} and in the region between 250 and 450 cm^{-1}), is observed above 10 GPa. These new bands were observed in RS measurements performed in different zones of the sample and the bands shift with increasing pressure at a similar rate to that of the first-order Raman modes (see Figure 5(right)), so they cannot be ascribed to solid oxygen.[78] In fact, one of them could be related to the B_{1g} vibrational mode theoretically predicted to be initially at 369.4 cm^{-1}. Since the recovered sample presents the same RS initial spectrum (see top RS spectrum in Figure 5(left)), it seems that all these bands come from the sample; so the hypothesis of sample decomposition is not valid to explain them. Besides, considerable disorder occurs in the sample on increasing pressure above 10 GPa, as will be discussed in the next section. Therefore, we have attributed the broad bands to second-order Raman modes and/or defect-activated Raman scattering corresponding to the PDOS as it occurs in a number of materials.[75,79,80] A comparison of the Raman spectrum at 23.4 GPa and the PDOS at 23.7 GPa (Figure S6 in the Supporting Information) shows that the second hypothesis is reasonable despite there are differences in frequency and intensity between the experimental and theoretical spectra which point to an overestimation of the frequencies of the high-frequency vibrational modes in theoretical calculations. It must be stressed that the RS spectrum of Bi_2O_2Se after pressure release from 28.3 GPa is similar to the original one. This means that no hint of the high-frequency phonons is observed despite the possible creation of pressure-induced defects, which can behave as electron trapping centers, as it occurs in ZnO after

Table 3. Experimental and Theoretical First-Order Raman (R) and Infrared (IR) Vibrational Mode Frequencies and Pressure Coefficients at Room Pressure in Bi_2O_2Se As Obtained by a Fit with the Equation $\omega(P) = \omega_0 + a \cdot P$ in the Pressure Range from 0 to 4 GPa*

	experimental		theoretical	
symmetry	ω_0 (cm^{-1})	a (cm^{-1}/GPa)	ω_0 (cm^{-1})	a (cm^{-1}/GPa)
E_u (IR)			59.2(3)	5.5(2)
A_{2u} (IR)			64.5(1)	4.1(9)
E_g (R)	59.5(5)	1.0(2)	72.0(1)	1.1(8)
A_{1g} (R)	160.5(6)	2.1(3)	165.7(3)	2.1(2)
E_u (IR)			293.9(1)	4.2(6)
B_g (R)			369.4(5)	4.0(5)
A_{2u} (IR)			402.8(6)	3.1(4)
E_g (R)			444.0(1)	5.3(7)
P1 (6.6 GPa)	137(3)	1.9(4)		
P2 (10.0 GPa)	280(8)	1.1(5)		
P3 (10.0 GPa)	285(7)	2.6(4)		
P4 (6.6 GPa)	296(4)	4.0(2)		
P5 (10.0 GPa)	381(7)	1.8(3)		
P6 (10.0 GPa)	447(5)	2.5(2)		
P7 (10.0 GPa)	537(8)	0.4(4)		
P8 (10.0 GPa)	568(6)	1.2(2)		

*The frequencies and pressure coefficients of other modes observed at different pressures (indicated) are also provided.

the highly reconstructive first-order wurtzite-to-rocksalt transition.[81]

Figure 5(right) shows the experimental and theoretical Raman-active mode frequencies of Bi_2O_2Se as a function of pressure up to 28.3 GPa and Table 3 summarizes the experimental and theoretical frequencies and pressure coefficients of the Raman-active modes of Bi_2O_2Se. As it can be observed, the pressure evolution of the experimental low-frequency Raman-active A_{1g} and E_g modes agrees well with our calculations despite theoretical frequencies are slightly overestimated. Moreover, the relative maxima of the broad band observed above 250 cm^{-1} also show similar pressure coefficients as the high-frequency modes. It is possible that the clear observation of several vibrational modes especially above 11.3 GPa could be related to the creation of defects in the sample around 10 GPa which also could be due to the loss of hydrostatic conditions of the pressure-transmitting medium and to the reduction of the phonon damping. In this context, more RS studies with samples of different concentrations are needed to shed light about the nature of these additional HP vibrational modes.

In summary, both HP-XRD and HP-RS measurements are in agreement with theoretical calculations and show that Bi_2O_2Se does not undergo any phase transition up to 30 GPa, unlike other isostructural Sillén-type compounds, which undergo a pressure-induced second-order tetragonal-to-collapsed tetragonal phase transition at relatively low pressures[32−37] and lead to significant changes of vibrational and elastic properties.[82]

4.3. Dynamical and Mechanical Stability of Bi_2O_2Se at HP. In order to verify that there is no hidden pressure-induced second-order phase transition, we have calculated the PDCs of Bi_2O_2Se along the main points of the BZ at 0, 12, and 23.7 GPa (Figure 6). As it can be observed, there are smooth changes of vibrational frequencies with increasing pressure, but there is no softening of vibrational modes (modes whose frequency goes to zero) which could lead to think about the existence of a dynamical instability of the tetragonal phase of Bi_2O_2Se and therefore the presence of a second-order phase transition in the whole pressure range up to 25 GPa.

In a complementary way, we have calculated the pressure dependence of the elastic stiffness constants also known as elastic constants (Figure S7 in Supporting Information) and studied the generalized stability criteria up to 45 GPa (Figure 7) for a body-centered tetragonal lattice (see Supporting Information for more details). Evidence of a mechanical instability of the tetragonal phase of Bi_2O_2Se is only observed around 41 GPa due to the decrease of the M_2 stability criterion. This result clearly shows that the body-centered tetragonal structure of Bi_2O_2Se is mechanically stable up to 41 GPa.

In a nutshell, we can conclude that our measurements and calculations clearly support the high structural stability of the tetragonal Sillén-type phase of Bi_2O_2Se under compression and the 2D character of the compound up to 30 GPa. It must be stressed that the high structural stability of body-centered tetragonal Bi_2O_2Se could be related to the behavior of the Bi LEPs. Bi LEPs, oriented toward the atomic Se layers in Bi_2O_2Se, are likely responsible for the 2D character of many Bi-containing compounds, as already commented. It has been shown that HP leads to strong compression of Bi LEPs in other Bi-based compounds, like β-Bi_2O_3,[29,77] and consequently leads to structural changes at relatively low pressures. Therefore, the large structural stability of layered Bi_2O_2Se can be understood by the relatively low compression of the Bi−Se distance in comparison to the decrease of the van der Waals interlayer distance in van der Waals-based layered compounds. In this way, there is a small distortion of Bi LEPs at HP that prevents strong structural changes as those observed in other Bi-based compounds.

4.4. Optical Absorption Measurements. Despite the interest that TE properties of chalcogenides have attracted, the number of detailed studies regarding their optical properties is scarce. Only very recently, the indirect bandgap of Bi_2O_2Se has been determined by angle-resolved photoelectron spectroscopy (ARPES) to be around 0.8 eV.[19] Figure 8 shows the optical absorption spectrum of a 3 μm-thick sample of Bi_2O_2Se at room conditions. The maximum value that the absorption coefficient reaches (~12 × 10^3 cm^{-1}) is typical of a direct bandgap. However, the relatively slow rise of the absorption

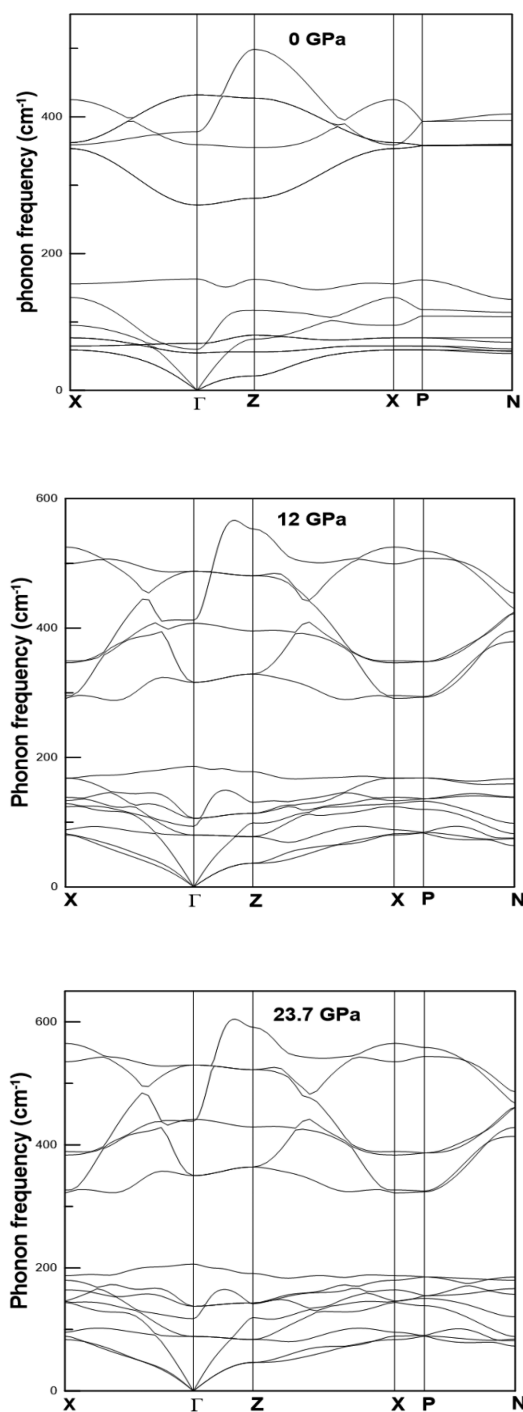**Figure 6.** Theoretical PDCs of Bi_2O_2Se at 0 GPa (top), 12 GPa (center), and 23.7 GPa (bottom) following the path X $(0,0,^1/_2) - \Gamma$ $(0,0,0) - Z$ $(^1/_2,^1/_2,-^1/_2) - P$ $(^1/_4,^1/_4,^1/_4) - N$ $(0,^1/_2,0)$.

Figure 7. Pressure dependence of generalized stability criteria of Bi_2O_2Se up to 45 GPa.

Figure 8. Optical absorption spectrum (black) of Bi_2O_2Se at ambient pressure fitted to a direct-type Urbach law (red). The inset shows the linear range presented by the absorption edge of Bi_2O_2Se considering either an indirect $(\alpha^{1/2})$ or a direct-type Urbach tail $(\ln(\alpha))$. The points are experimental data while the straight red lines are guides for the eye.

edge that extends for 0.5 eV resembles either the absorption edge of an indirect bandgap, where $\alpha \sim (h\nu - E_g)^2$, or the low-energy exponential absorption tail of a direct transition, as described by the Urbach law.[83] In the case of Urbach's tail, the absorption coefficient can be described by $\alpha = A_0 \times \exp[(h\nu - E_g)/E_U]$, where A_0 is an intrinsic constant of the material, E_U is Urbach's energy and relates to the steepness of the absorption edge, and E_g is the bandgap. In the inset of Figure 8, Tauc plots with the energy dependence of both the $\ln(\alpha)$ and $\alpha^{1/2}$ are shown to clarify this issue.[84,85] We find a longer straight linear range with $\ln(\alpha)$ than with $\alpha^{1/2}$; thus suggesting that the optical
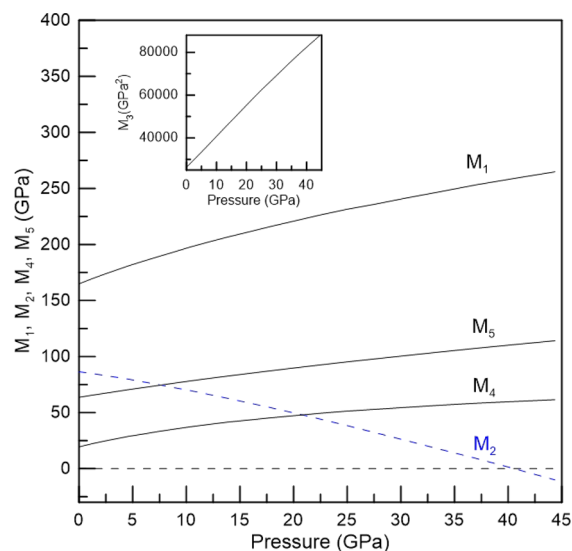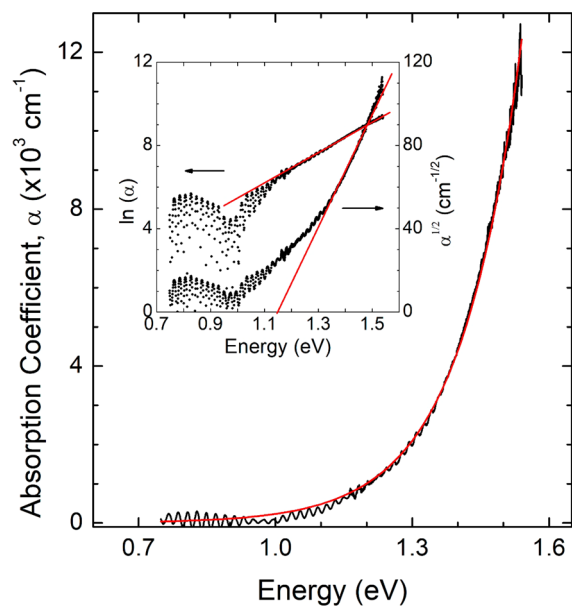
bandgap of Bi_2O_2Se is most likely direct, with a value $E_g = 1.486$ eV, and its low energy absorption tail follows an Urbach's law. This is also demonstrated by the remarkable agreement between our experimental and simulated spectra (Figure 8) that provides values of $A_0 = 8300$ cm^{-1} and $E_U = 0.136$ eV once the direct bandgap value is fixed.

The theoretical electronic band structure of bulk Bi_2O_2Se calculated with DFT GGA-PBEsol including SOC at 0 GPa is shown at the top of Figure 9. Our calculations exhibit the minimum of the conduction band (CB) at the Γ point and the maximum of the valence band (VB) at the N point. Other two local maxima of the VB are located along the $Z-X-\Gamma$ directions. According to our calculations, the bandgap of
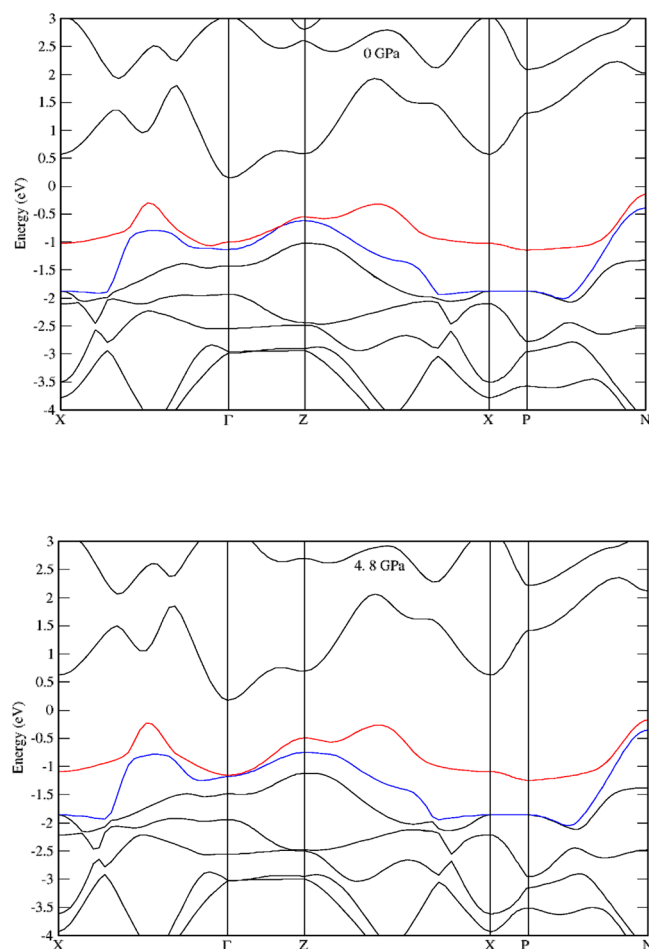
Figure 10. Optical absorption edge of Bi_2O_2Se on increasing pressure up to 20 GPa.

creation of defects as we will further comment. In summary, the optical bandgap of Bi_2O_2Se shows a particular behavior that can be divided into three steps. First the bandgap blueshifts up to 5 GPa with a pressure coefficient of $dE_g/dP = 29$ meV/GPa. This is followed by a pressure-independent behavior from 5 to 15 GPa and finally a redshift with $dE_g/dP = −13$ meV/GPa, accompanied by an abrupt increase of Urbach's energy.

The HP evolution of the experimental optical bandgap and Urbach's energy E_U up to 20 GPa are shown in Figure 11,

Figure 9. Electronic band structure of Bi_2O_2Se at (top) 0 and 4.8 GPa (bottom) following the path: X $(0,0,^1/_2)$ − Γ $(0,0,0)$ − Z $(^1/_2,^1/_2,−^1/_2)$ − P $(^1/_4,^1/_4,^1/_4)$ − N $(0,^1/_2,0)$. Topmost valence bands (in red) and second topmost valence bands (in blue) are colored in order to better show the crossing and anticrossing taking place in these bands with increasing pressure around 4 GPa.

Bi_2O_2Se is indirect $(N−\Gamma)$ with a value of 0.296 eV and the direct bandgaps of lower energy are located at Z (1.13 eV) and Γ (1.15 eV) points of the BZ. When compared with the indirect bandgap obtained from ARPES measurements (0.8 eV),[19] it can be observed that our calculations underestimate the indirect bandgap by 0.5 eV. Taking into account this underestimation of the bandgap, we can estimate from our calculations that the real direct optical transitions are expected around 1.4−1.6 eV; thus in good agreement with our optical absorption measurements at room pressure.

In order to study the HP behavior of the optical bandgap and check the nature of the direct gap, we have performed optical absorption experiments at HP (see Figure 10). As pressure increases, the absorption edge keeps its shape and shifts to higher energies up to ∼5 GPa. Above this pressure, the absorption edge becomes insensitive to pressure with the sample keeping its optical quality as evidenced by the persistence of interference fringes at the low-energy range due to the Fabry−Pérot cavity created by the sample. At ∼15 GPa, in agreement with the appearance of extra vibrational bands observed before by RS spectroscopy, the fringes vanish, the low-energy tail grows, and the edge appears to shift to low energies. This might be indicative of the pressure-induced
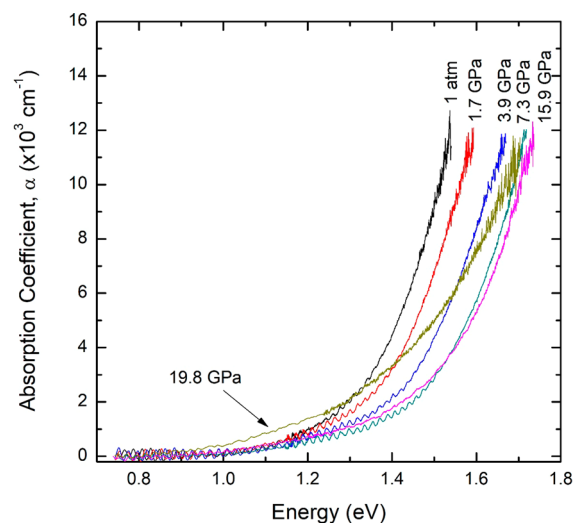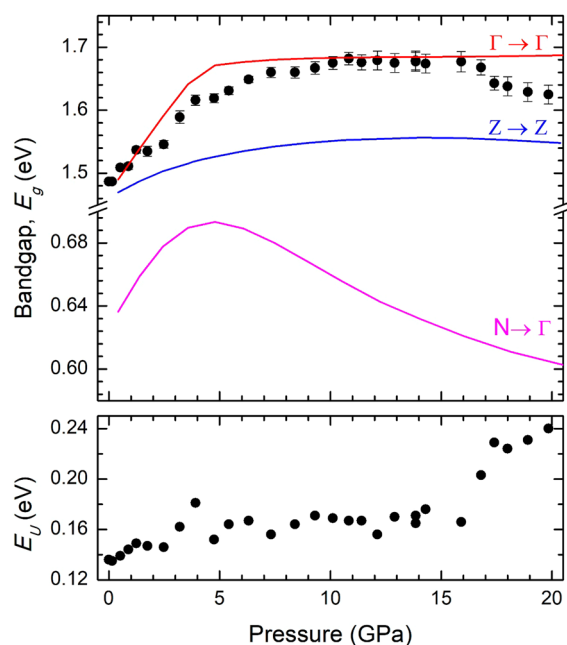

Figure 11. (Top) Pressure dependence of the band gap of Bi_2O_2Se obtained from fitting the absorption edge to the Urbach's law. Dots represent the experimental data and the continuous lines are the calculated dependences for the $\Gamma \rightarrow \Gamma$ (red line) and the $Z \rightarrow Z$ (blue line) direct transitions after adding +0.34 eV to compare to the experimentally observed bandgap at ambient pressure. The theoretical $N−\Gamma$ indirect bandgap of Bi_2O_2Se is also shown for comparison (pink line). (Bottom) Pressure dependence of the Urbach energy in Bi_2O_2Se.
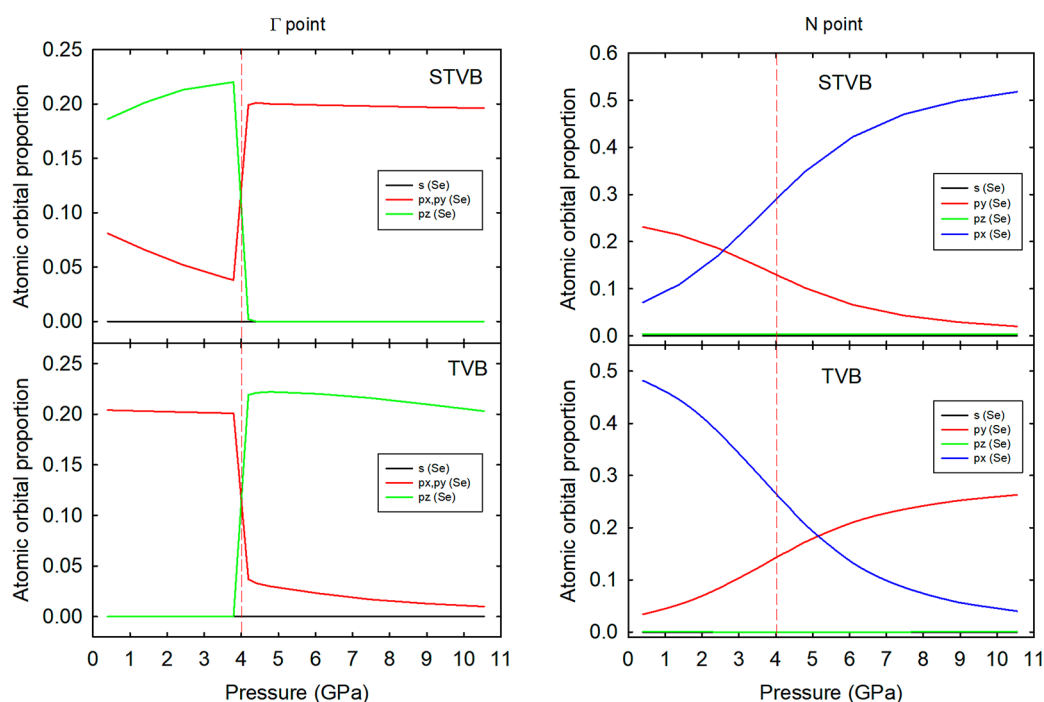
Figure 12. Pressure evolution of the Se orbitals contribution in the top valence bands at (left) Γ and (right) N points. The sudden change of character of topmost valence bands at Γ is indicative of a band crossing while the progressive change of character of topmost valence bands at N is indicative of a band anticrossing.

where they are compared to the calculated pressure dependence of the indirect N−Γ bandgap and the two lowermost direct Z−Z and Γ−Γ transitions. On one hand, the behavior of the experimental optical bandgap is qualitatively similar to that of the direct bandgap at the Γ point. In order to show it more clearly, the theoretical values have been increased by 0.34 eV so that the theoretical direct bandgap at Γ matches the experimental value of the optical direct bandgap at 0 GPa. On the other hand, the indirect transition shows a maximum at 5 GPa and then slowly redshifts with pressure, while the pressure dependence of the direct Z transition is also similar to the experimental behavior, but with a much smaller pressure coefficient. Therefore, our results confirm that Bi_2O_2Se has an indirect bandgap that can be estimated around ∼0.8 eV if a shift of 0.5 eV is added to our calculations and a direct optical bandgap around 1.49 eV. The reason for not observing optically the indirect N-Γ transition and the direct transition at Z could be related to their forbidden character (the minimum of the CB is mainly contributed by p orbitals of Bi) or to their very low absorption coefficient so that the optical direct bandgap at Γ is the one observed experimentally.

Above 15 GPa, our calculations do not reproduce the redshift experimentally observed (Figure 11(top)). We believe that the experimentally observed redshiftting tail is due to the progressive creation of defects above 10 GPa. The deterioration of the sample above 15 GPa is evident by the disappearance of interference fringes in the optical absorption measurements (Figure 10), and Urbach's model allows us to indirectly quantify such effect with Urbach's energy E_U, as shown in Figure 11(bottom). Up to 15 GPa, E_U takes a value of ∼160 meV, which is already high and similar to that of disordered systems as indium thiospinels;[86,87] however, above 15 GPa, the value of E_U increases up to 240 meV at 20 GPa, which indicates that the number of defects increases abruptly above 15 GPa and making optical absorption measurements very difficult above 20

GPa. Therefore, we ascribe the decrease of the optical bandgap in Bi_2O_2Se above 15 GPa to the creation of defects that produce levels between the VB and CB, thus decreasing the optical bandgap. In this respect, the decrease of pressure allows to show the reversibility of the change of the optical bandgap, but the sample is so damaged that interference fringes are no longer observed.

It is interesting to notice the change of the pressure dependence exhibited by both the direct and indirect bandgaps between 4 and 5 GPa with an abrupt change of their pressure coefficients. In order to understand these phenomena, we have compared in Figure 9 the theoretical electronic band structure of bulk Bi_2O_2Se at 0 and 4.8 GPa. The electronic density of states (DOS) at both pressures is also provided as Figure S9 in the Supporting Information. As it can be observed, the two topmost VBs at Γ are closer at 4.8 GPa than at 0 GPa. In fact, they cross each other around 4 GPa. This crossing explains the abrupt change in pressure coefficient of the direct gap between 4 and 5 GPa. This effect can be better seen in Figure 12(left) where the pressure dependence of the orbital decomposition of the topmost VB (TVBs) and the second topmost VB (STVBs) are shown. At room pressure, the TVB in Bi_2O_2Se at Γ is mainly contributed by the p_x and p_y orbitals of Se while the STVB is mainly contributed by the p_z orbital of Se. Since STVB has a larger pressure coefficient than TVB, they come close to each other and a crossing of these bands occurs at 4 GPa. Above that pressure, the presence of the p_x and p_y orbitals at the TVB almost decreases to zero and the p_z orbital is the main responsible for these bands at higher pressures. The contrary occurs to STVB so the energy distance between TVB and STBV increases above 4 GPa. This abrupt change is a clear indication of a band crossing. The larger pressure coefficient of bands with p_z character than of bands with p_x and p_y character is similar to that of the conduction band at Γ (also with p_z

character) so the pressure coefficient of the direct bandgap is positive (negligible) below (above) 5 GPa.

Similarly, the indirect bandgap $N-\Gamma$ (Figure 11) presents a change in the pressure coefficient (a maximum value in energy is obtained around 4.8 GPa). As in the case of the direct bandgap, the change in pressure coefficient of the $N-\Gamma$ indirect bandgap can be understood by the change of the character of the two topmost VBs at the N point with increasing pressure. At ambient pressure, the TVB at the N point is mainly contributed by p_x and p_y orbitals of Se (Figure 12(right)), being the p_x orbital contribution more than 10 times higher than the p_y one. On the other hand, the STVB at the N point is of the same symmetry and has similar orbital contribution of p_x and p_y orbitals of Se; however, in this case the p_y orbital contribution is around 2.5 times higher than the p_x one. Since STVB has a larger pressure coefficient than TVB, they become closer in energy with increasing pressure, reaching a minimum energy distance around 5.0 GPa, and tend to separate at higher pressures. This is typical of a band anticrossing since both bands have the same character.[88] At the same time, a progressive variation of the contributions of p_x and p_y orbitals of Se in both VBs occur as they come closer. In fact, the proportion of p_y character in the TVB becomes larger than that of p_x character above 5.0 GPa and the contrary occurs in the STVB, where the proportion of p_x character becomes larger than that of p_y character above 2.5 GPa. These continuous changes of character are indicative of an anticrossing of the two topmost VBs at the N point around 4 GPa. In summary, we can conclude that these crossings and anticrossings observed in the top of the VB of Bi_2O_2Se are related to the high compressibility of the Bi−Se bonds as compared with the Bi−O bonds. Note that the evolution of the Bi−Se distance with pressure (Figure 4) shows a pressure coefficient of -14.8×10^{-3} Å/GPa in the range from 0 to 4 GPa and a pressure coefficient of -8.2×10^{-3} Å/GPa in the range of 10 to 16 GPa; thus indicating that the bond Bi−Se becomes almost half as compressible at 10 GPa than at room pressure. This is a consequence of the 2D layered character of Bi_2O_2Se (Figure 1(top)); therefore, we can ascribe the changes observed near 4 GPa in RS measurements to changes in the electronic band structure related to the strong compression of the interlayer distance and therefore affecting considerably to Se atoms. Finally, it must be stressed that the change of the character of the TVB at the N point around 4 GPa could lead to a pressure-induced electronic topological transition (ETT) if p-type doping of Bi_2O_2Se is achieved.

5. CONCLUSIONS

Our joint experimental and theoretical study of the structural, vibrational, optical, elastic, and electronic properties of layered Bi_2O_2Se under compression has shown a good agreement between experiments and *ab initio* calculations for the EOS, the pressure coefficients of the Raman-active modes and the bandgap of this material. The compressibility and vibrational properties of this layered compound based on weak interlayer electrostatic interactions has been analyzed and discussed in comparison with typical layered compounds based on van der Waals interlayer forces. In particular, the vibrational properties of Bi_2O_2Se have been discussed in detail on the light of the correct Brillouin zone for Sillén-type compounds.

No first- or second-order phase transition has been observed in Bi_2O_2Se up to 30 GPa. Therefore, this material is one of the more stable Sillén-type compounds under compression. Curiously, the Bi-based compound $BiSbO_4$ has been recently

found to be stable up to 70 GPa.[89] Despite the lack of important structural changes at high pressure, Bi_2O_2Se exhibits interesting electronic changes around 4 GPa, which are mainly related to the shortening and hardening of the long Bi−Se bonds, and leads to a strong change in the vibrational, optical and electronic properties of the material due to a change of the character of the topmost valence bands. We hope this work will stimulate further studies of Bi_2O_2Se and will help to shed light over this high-mobility semiconductor in order to enhance the interesting electronic and TE properties of bismuth oxy-chalcogenides. Furthermore, the results here reported for Bi_2O_2Se will be helpful to understand the properties of other layered Sillén-type compounds and in general in other layered materials lacking van der Waals forces between their layers. In particular, this study will be interesting to understand the behavior under pressure of Sb-based Sillén-type compounds[32] whose properties under pressure have not been explored to our knowledge.

■ ASSOCIATED CONTENT

ⓈSupporting Information

The Supporting Information is available free of charge on the ACS Publications website at DOI: 10.1021/acs.jpcc.8b02194.

Experimental lattice parameters and unit cell volumes of Bi_2O_2Se at different pressures; visualization of the vibrational modes at the Γ point; evolution with pressure of the theoretical infrared active (IR-active) modes, elastic constants, C_{ij}, and elastic stiffness, B_{ij}, of Bi_2O_2Se; and electronic density of states (DOS) of Bi_2O_2Se at 0 and 4.8 GPa (PDF)

■ AUTHOR INFORMATION

Corresponding Authors
*(A.L.J.P.) E-mail: andrepereira@ufgd.edu.br.
*(F.J.M.) E-mail: fjmanjon@fis.upv.es.

ORCID ⓘ
A. L. J. Pereira: 0000-0003-4757-8080
D. Santamaría-Pérez: 0000-0002-1119-5056
V. P. Cuenca-Gotor: 0000-0003-0819-8528
R. Vilaplana: 0000-0003-0504-2157
O. Gomis: 0000-0001-6763-0638
L. Gracia: 0000-0001-9684-2568

Notes
The authors declare no competing financial interest.

■ REFERENCES

(1) Xia, Y.; Qian, D.; Hsieh, D.; Wray, L.; Pal, A.; Lin, H.; Bansil, A.; Grauer, D.; Hor, Y. S.; Cava, R. J.; et al. Discovery (Theoretical Prediction and Experimental Observation) of a Large-Gap Topological-Insulator Class with Spin-Polarized Single-Dirac-Cone on the Surface. *Nat. Phys.* **2009**, *5*, 398−402.

(2) Zhang, H.; Liu, C. X.; Qi, X. L.; Dai, X.; Fang, Z.; Zhang, S. C. Topological Insulators in Bi_2Se_3, Bi_2Te_3 and Sb_2Te_3 With a Single Dirac Cone on the Surface. *Nat. Phys.* **2009**, *5*, 438−442.

(3) Chen, Y. L.; Analytis, J. G.; Chu, J.-H.; Liu, Z. K.; Mo, S.-K.; Qi, X. L.; Zhang, H. J.; Lu, D. H.; Dai, X.; Fang, Z.; et al. Experimental Realization of a Three-Dimensional Topological Insulator, Bi_2Te_3. *Science* **2009**, *325*, 178−181.

(4) Hsieh, D.; Xia, Y.; Qian, D.; Wray, L.; Meier, F.; Dil, J. H.; Osterwalder, J.; Patthey, A.; Fedorov, A. V.; Lin, H.; et al. Observation of Time-Reversal-Protected Single-Dirac-Cone Topological-Insulator States in Bi_2Te_3 and Sb_2Te_3. *Phys. Rev. Lett.* **2009**, *103*, 146401.

(5) König, M.; Wiedmann, S.; Brüne, C.; Roth, A.; Buhmann, H.; Molenkamp, L. W.; Qi, X.-L.; Zhang, S.-C. Quantum Spin Hall Insulator State in HgTe Quantum Wells. *Science* **2007**, *318*, 766−770.

(6) Chang, C.-Z.; Zhang, J.; Feng, X.; Shen, J.; Zhang, Z.; Guo, M.; Li, K.; Ou, Y.; Wei, P.; et al. Experimental Observation of the Quantum Anomalous Hall Effect in a Magnetic Topological Insulator. *Science* **2013**, *340*, 167−170.

(7) Fu, L.; Kane, C. L. Superconducting Proximity Effect and Majorana Fermions at the Surface of a Topological Insulator. *Phys. Rev. Lett.* **2008**, *100*, 096407.

(8) Yue, Z.; Cai, B.; Wang, L.; Wang, X.; Gu, M. Intrinsically Core-Shell Plasmonic Dielectric Nanostructures with Ultrahigh Refractive Index. *Sci. Adv.* **2016**, *2*, e1501536.

(9) Yue, Z.; Xue, G.; Liu, J.; Wang, Y.; Gu, M. Nanometric Holograms Based on a Topological Insulator Material. *Nat. Commun.* **2017**, *8*, 15354.

(10) Yang, J. *Prospective Thermoelectrics among Topological Insulators, Materials Aspect of Thermoelectricity*; Uher, C., Ed.; CRC: Boca Raton, FL, 2017.

(11) Rowe, D. M. *CRC Handbook of Thermoelectrics*; CRC Press Inc.: New York, 1995.

(12) Venkatasubramanian, R.; Siivola, E.; Colpitts, T.; O'Quinn, B. Thin-Film Thermoelectric Devices with High Room-Temperature Figures of Merit. *Nature* **2001**, *413*, 597−602.

(13) Mahan, G. D. Figure of Merit for Thermoelectrics. *J. Appl. Phys.* **1989**, *65*, 1578−1583.

(14) Harman, T. C.; Taylor, P. J.; Walsh, M. P.; LaForge, B. E. Quantum Dot Superlattice Thermoelectric Materials and Devices. *Science* **2002**, *297*, 2229−2232.

(15) Ruleova, P.; Drasar, C.; Lostak, P.; Li, C. P.; Ballikaya, S.; Uher, C. Thermoelectric Properties of Bi_2O_2Se. *Mater. Chem. Phys.* **2010**, *119*, 299−302.

(16) Guo, D.; Hu, C.; Xi, Y.; Zhang, K. Strain Effects to Optimize Thermoelectric Properties of Doped Bi_2O_2Se via Tran − Blaha Modified Becke − Johnson Density Functional Theory. *J. Phys. Chem. C* **2013**, *117*, 21597−21602.

(17) Tan, X.; Lan, J.-L.; Ren, G.; Liu, Y.; Lin, Y.-H.; Nan, C.-W. Enhanced Thermoelectric Performance of N-Type Bi_2O_2Se by Cl-Doping at Se Site. *J. Am. Ceram. Soc.* **2017**, *100*, 1494−1501.

(18) Tan, X.; Liu, Y.; Hu, K.; Ren, G.; Li, Y.; Liu, R.; Lin, Y.-H.; Lan, J.-L.; Nan, C.-W. Synergistically Optimizing Electrical and Thermal Transport Properties of Bi_2O_2Se Ceramics by Te-Substitution. *J. Am. Ceram. Soc.* **2018**, *101*, 326−333.

(19) Wu, J.; Yuan, H.; Meng, M.; Chen, C.; Sun, Y.; Chen, Z.; Dang, W.; Tan, C.; Liu, Y.; Yin, J.; et al. High Electron Mobility and Quantum Oscillations in Non-Encapsulated Ultrathin Semiconducting Bi_2O_2Se. *Nat. Nanotechnol.* **2017**, *12*, 530−534.

(20) Wu, J. X.; Tan, C. W.; Tan, Z. J.; Liu, Y. J.; Yin, J. B.; Dang, W. H.; Wang, M. Z.; Peng, H. L. Controlled Synthesis of High-Mobility Atomically Thin Bismuth Oxyselenide Crystals. *Nano Lett.* **2017**, *17*, 3021−3026.

(21) Wu, J.; Liu, Y.; Tan, Z.; Tan, C.; Yin, J.; Li, T.; Tu, T.; Peng, H. Chemical Patterning of High-Mobility Semiconducting 2D Bi_2O_2Se Crystals for Integrated Optoelectronic Devices. *Adv. Mater.* **2017**, *29*, 1704060.

(22) Wu, M.; Zeng, X. C. Bismuth Oxychalcogenides: A New Class of Ferroelectric/Ferroelastic Materials with Ultra High Mobility. *Nano Lett.* **2017**, *17*, 6309−6314.

(23) Shevelkov, A. V.; Shatruk, M. M. Mercury and Cadmium pnictide-halides: The Inverted Zintl Phases. *Russ. Chem. Bull.* **2001**, *50*, 337−352.

(24) Vegas, A.; Santamaria-Perez, D. The Structures of ZrNCl, TiOCl and AlOCl in the Light of the Zintl-Klemm Concept. *Z. Kristallogr. - Cryst. Mater.* **2003**, *218*, 466−469.

(25) Leciejewicz, J. On the Crystal Structure of Tetragonal (red) PbO. *Acta Crystallogr.* **1961**, *14*, 1304.

(26) Manjón, F. J.; Vilaplana, R.; Gomis, O.; Pérez-González, E.; Santamaría-Pérez, D.; Marín-Borrás, V.; Segura, A.; González, J.; Rodríguez-Hernández, P.; Muñoz, A.; et al. High-pressure Studies of Topological Insulators Bi_2Se_3, Bi_2Te_3, and Sb_2Te_3. *Phys. Status Solidi B* **2013**, *250*, 669−676.

(27) Pereira, A. L. J.; Errandonea, D.; Beltrán, A.; Gracia, L.; Gomis, O.; Sans, J. A.; García-Domene, B.; Miquel-Veyrat, A.; Manjón, F. J.; Muñoz, A.; et al. Structural Study of α-Bi_2O_3 under Pressure. *J. Phys.: Condens. Matter* **2013**, *25*, 475402.

(28) Pereira, A. L. J.; Gomis, O.; Sans, J. A.; Pellicer-Porres, J.; Manjón, F. J.; Beltran, A.; Rodríguez-Hernandez, P.; Muñoz, A. Pressure Effects on the Vibrational Properties of α-Bi_2O_3: An Experimental and Theoretical Study. *J. Phys.: Condens. Matter* **2014**, *26*, 225401.

(29) Pereira, A. L. J.; Sans, J. A.; Vilaplana, R.; Gomis, O.; Manjón, F. J.; Rodríguez-Hernández, P.; Muñoz, A.; Popescu, C.; Beltrán, A. Isostructural Second-Order Phase Transition of β-Bi_2O_3 at High Pressures: An Experimental and Theoretical Study. *J. Phys. Chem. C* **2014**, *118*, 23189.

(30) Ibañez, J.; Sans, J. A.; Popescu, C.; López-Vidrier, J.; Elvira-Betanzos, J. J.; Cuenca-Gotor, V. P.; Gomis, O.; Manjón, F. J.; Rodríguez-Hernández, P.; Muñoz, A. Structural, Vibrational, and Electronic Study of Sb_2S_3 at High Pressure. *J. Phys. Chem. C* **2016**, *120*, 10547.

(31) Loa, I.; Bos, J.-W. G.; Downie, R. A.; Syassen, K. Atomic Ordering in Cubic Bismuth Telluride Alloy Phases at High Pressure. *Phys. Rev. B: Condens. Matter Mater. Phys.* **2016**, *93*, 224109.

(32) Huhnt, C.; Michels, G.; Roepke, M.; Schlabitz, W.; Wurth, A.; Johrendt, D.; Mewis, A. First-Order Phase Transitions in the $ThCr_2Si_2$-type Phosphides ARh_2P_2 (A = Sr, Eu). *Phys. B* **1997**, *240*, 26−37.

(33) Huhnt, C.; Schlabitz, W.; Wurth, A.; Mewis, A.; Reehuis, M. First- and Second-Order Phase Transitions in Ternary Europium Phosphides with $ThCr_2Si_2$-type Structure. *Phys. B* **1998**, *252*, 44−54.

(34) Li, Y. Y.; Ni, J. The stable $CaBe_2Ge_2$ Structures in Antimonide Compounds ATM_2Sb_2 (A = Ca, Sr, Ba; TM = Fe, Co, Ni, Cu): A First-Principles Study. *Phys. Lett. A* **2011**, *375*, 4218−4224.

(35) Sefat, A. S. Pressure Effects on Two Superconducting Iron-Based Families. *Rep. Prog. Phys.* **2011**, *74*, 124502−124516.

(36) Sun, L.; Chen, X.-J.; Guo, J.; Gao, P.; Huang, Q.-Z.; Wang, H.; Fang, M.; Chen, X.; Chen, G.; Wu, Q.; Zhang, C.; et al. Re-Emerging Superconductivity at 48 K in Iron Chalcogenides. *Nature* **2012**, *483*, 67−69.

(37) Das, T.; Balatsky, A. V. Origin of Pressure Induced Second Superconducting Dome in A_yFe_2−xSe_2 [A = K, (Tl,Rb)]. *New J. Phys.* **2013**, *15*, 093045−093057.

(38) Wang, Y. Q.; Lu, P. C.; Wu, J. J.; Liu, J.; Wang, X. C.; Zhao, J. Y.; Bi, W.; Alp, E. E.; Park, C. Y.; Popov, D.; et al. Phonon Density of States of Single-Crystal $SrFe_2As_2$ across the Collapsed Phase Transition at High Pressure. *Phys. Rev. B: Condens. Matter Mater. Phys.* **2016**, *94*, 014516.

(39) Vilaplana, R.; Santamaría-Pérez, D.; Gomis, O.; Manjón, F. J.; González, J.; Segura, A.; Muñoz, A.; Rodríguez-Hernández, E.; Pérez-González, E.; Marín-Borrás, V.; et al. Structural and Vibrational Study

of Bi_2Se_3 under High Pressure. *Phys. Rev. B: Condens. Matter Mater. Phys.* **2011**, *84*, 184110.

(40) Ruleova, P.; Drasar, C.; Benes, L.; Lostak, P.; Li, C.-P.; Kong, H.; Uher, C. Bi_2O_2Se − A Prospective Thermoelectric Material? *6th Eur. Conf. Thermoelectr.* **2009**, P2−35.

(41) Boller, H. Die Kristallstruktur von Bi_2O_2Se. *Monatsh. Chem.* **1973**, *104*, 916−919.

(42) Raccah, P. M.; Longo, J. M.; Eick, H. A. The Crystal Structure of Neodymium Monotellurooxide-Nd_2O_2Te. *Inorg. Chem.* **1967**, *6*, 1471−1473.

(43) Luu, S. D. N.; Vaqueiro, P. Synthesis, Characterization and Thermoelectric Properties of the Oxytelluride Bi_2O_2Te. *J. Solid State Chem.* **2015**, *226*, 219−223.

(44) Merrill, L.; Bassett, W. A. Miniature Diamond Anvil Pressure Cell for Single Crystal X-Ray Diffraction Studies. *Rev. Sci. Instrum.* **1974**, *45*, 290−294.

(45) Mao, H. K.; Xu, J.; Bell, P. M. Calibration of the Ruby Pressure Gauge to 800 Kbar under Quasi-Hydrostatic Conditions. *J. Geophys. Res.* **1986**, *91*, 4673−4676.

(46) Fauth, F.; Peral, I.; Popescu, C.; Knapp, M. The New Material Science Powder Diffraction Beamline at ALBA Synchrotron. *Powder Diffr.* **2013**, *28*, S360−S370.

(47) Dewaele, A.; Loubeyre, P.; Mezouar, M. Equations of State of Six Metals Above 94 GPa. *Phys. Rev. B: Condens. Matter Mater. Phys.* **2004**, *70*, 094112.

(48) Prescher, C.; Prakapenka, V. B. DIOPTAS: A Program for Reduction of Two-Dimensional X-Ray Diffraction Data and Data Exploration. *High Pressure Res.* **2015**, *35*, 223−230.

(49) Rodriguez-Carvajal, J. Recent Advances in Magnetic Structure Determination by Neutron Powder Diffraction. *Phys. B* **1993**, *192*, 55−69.

(50) Nolze, G.; Kraus, W. PowderCell 2.0 for Windows. *Powder Diffr.* **1998**, *13*, 256−259.

(51) Letoullec, R.; Pinceaux, J. P.; Loubeyre, P. The Membrane Diamond Anvil Cell: A New Device for Generating Continuous Pressure and Temperature Variations. *High Pressure Res.* **1988**, *1*, 77−90.

(52) Goñi, A. R.; Syassen, K. In *High Pressure Semiconductor Physics I*; Suski, T., Paul, W., Eds.; Academic Press: 1998; Chapter 4.

(53) Klotz, S.; Chervin, J.-C.; Munsch, P.; Le Marchand, G. Hydrostatic Limits of 11 Pressure Transmitting Media. *J. Phys. D: Appl. Phys.* **2009**, *42*, 075413.

(54) Errandonea, D.; Muñoz, A.; Gonzalez-Platas, J. Comment on "High-Pressure X-Ray Diffraction Study of YBO_3/Eu^{3+}, $GdBO_3$, and $EuBO_3$: Pressure-Induced Amorphization in $GdBO_3$. *J. Appl. Phys.* **2014**, *115*, 216101; *J. Appl. Phys.* **2014**, *115*, 216101.

(55) Hohenberg, P.; Kohn, W. Inhomogeneous Electron Gas. *Phys. Rev.* **1964**, *136*, B864−B871.

(56) Kresse, G.; Hafner, J. Ab Initio Molecular Dynamics for Liquid Metals. *Phys. Rev. B: Condens. Matter Mater. Phys.* **1993**, *47*, 558−561.

(57) Blöchl, P. E. Projector Augmented-Wave Method. *Phys. Rev. B: Condens. Matter Mater. Phys.* **1994**, *50*, 17953−17979.

(58) Perdew, J. P.; Ruzsinszky, A.; Csonka, G. I.; Vydrov, O. A.; Scuseria, G. E.; Constantin, L. A.; Zhou, X.; Burke, K. Restoring the Density-Gradient Expansion for Exchange in Solids and Surfaces. *Phys. Rev. Lett.* **2008**, *100*, 136406.

(59) Monkhorst, H. J.; Pack, J. D. Special Points for Brillouin-zone integrations. *Phys. Rev. B* **1976**, *13*, 5188−5192.

(60) Van Quang, T.; Lim, H.; Kim, M. Temperature and Carrier-Concentration Dependences of the Thermoelectric Properties of Bismuth Selenide Dioxide Compounds. *J. Korean Phys. Soc.* **2012**, *61*, 1728−1731.

(61) Van Quang, T.; Kim, M. Role of O and Se Defects in the Thermoelectric Properties of Bismuth Oxide Selenide. *J. Appl. Phys.* **2016**, *120*, 195105.

(62) Bradly, C. J.; Cracknell, A. P. *The Mathematical Theory of Symmetry in Solids*; Clarendon Press: Oxford, U.K., 1972.

(63) Aroyo, M. I.; Orobengoa, D.; de la Flor, G.; Tasci, E. S.; Perez-Mato, J. M.; Wondratschek, H. Brillouin-zone Database on the Bilbao

Crystallographic Server. *Acta Crystallogr., Sect. A: Found. Adv.* **2014**, *70*, 126−137.

(64) Parlinski, K. Computer Code PHONON. See: http://wolf.ifj.edu.pl/phonon.

(65) Nielsen, O. H.; Martin, R. M. Quantum-mechanical Theory of Stress and Force. *Phys. Rev. B: Condens. Matter Mater. Phys.* **1985**, *32*, 3780−3791.

(66) Le Page, Y.; Saxe, P. Symmetry General Least-Squares Extraction of Elastic Data for Strained Materials From ab Initio Calculations of Stress. *Phys. Rev. B: Condens. Matter Mater. Phys.* **2002**, *65*, 104104.

(67) Fujihisa, H.; Akahama, Y.; Kawamura, H.; Ohishi, Y.; Shimomura, O.; Yamawaki, H.; Sakashita, M.; Gotoh, Y.; Takeya, S.; Honda, K. O8 Cluster Structure of the Epsilon Phase of Solid Oxygen. *Phys. Rev. Lett.* **2006**, *97* (8), 085503.

(68) Lundegaard, L. F.; Weck, G.; McMahon, M. I.; Desgreniers, S.; Loubeyre, P. Observation of an O_8 Molecular Lattice in the Epsilon Phase of Solid Oxygen. *Nature* **2006**, *443*, 201−204.

(69) Birch, F. J. Finite Strain Isotherm and Velocities for Single-Crystal and Polycrystalline NaCl at High Pressures and 300K. *J. Geophys. Res.* **1978**, *83*, 1257−1268.

(70) Sakai, N.; Kajiwara, T.; Takemura, K.; Minomura, S.; Fujii, Y. Pressure-Induced Phase Transition in Sb_2Te_3. *Solid State Commun.* **1981**, *40*, 1045−1047.

(71) Polian, A.; Gauthier, M.; Souza, S. M.; Triches, D. M.; Cardoso de Lima, J.; Grandi, T. A. Two-Dimensional Pressure-Induced Electronic Topological Transition in Bi_2Te_3. *Phys. Rev. B: Condens. Matter Mater. Phys.* **2011**, *83*, 113106.

(72) Kroumova, E.; Aroyo, M. I.; Perez Mato, J. M.; Kirov, A.; Capillas, C.; Ivantchev, S.; Wondratschek, H. Bilbao Crystallographic Server: Useful Databases and Tools for Phase Transitions Studies. *Phase Transitions* **2003**, *76*, 155−170.

(73) Canepa, P.; Hanson, R. M.; Ugliengo, P.; Alfredsson, M. J-ICE: A New Jmol Interface for Handling and Visualizing Crystallographic and Electronic Properties. *J. Appl. Crystallogr.* **2011**, *44*, 225−229.

(74) Lockwood, D. J.; Yu, G.; Rowell, N. L. Optical Phonon Frequencies and Damping in AlAs, GaP, GaAs, InP, InAs and InSb Studied by Oblique Incidence Infrared Spectroscopy. *Solid State Commun.* **2005**, *136*, 404−409.

(75) Ibáñez, J.; Oliva, R.; Manjón, F. J.; Segura, A.; Yamaguchi, T.; Nanishi, Y.; Cusco, R.; Artus, L. High-Pressure Lattice Dynamics in Wurtzite and Rocksalt Indium Nitride Investigated by Means of Raman Spectroscopy. *Phys. Rev. B: Condens. Matter Mater. Phys.* **2013**, *88*, 115202.

(76) Hauber, A.; Fahy, S. Scattering of Carriers by Coupled Plasmon-Phonon Modes in Bulk Polar Semiconductors and Polar Semiconductor Heterostructures. *Phys. Rev. B: Condens. Matter Mater. Phys.* **2017**, *95*, 045210.

(77) Pereira, A. L. J.; Gomis, O.; Sans, J. A.; Contreras-García, J.; Manjón, F. J.; Rodríguez-Hernández, P.; Muñoz, A.; Beltrán, A. β-Bi_2O_3 Under Compression: Optical and Elastic Properties and Electron Density Topology Analysis. *Phys. Rev. B: Condens. Matter Mater. Phys.* **2016**, *93*, 224111.

(78) Akahama, Y.; Kawamura, H. High-Pressure Raman Spectroscopy of Solid Oxygen. *Phys. Rev. B: Condens. Matter Mater. Phys.* **1996**, *54*, R15602−R15605.

(79) Halsall, M. P.; Harmer, P.; Parbrook, P. J.; Henley, S. J. Raman Scattering and Absorption Study of the High-Pressure Wurtzite to Rocksalt Phase Transition of GaN. *Phys. Rev. B: Condens. Matter Mater. Phys.* **2004**, *69*, 235207.

(80) Manjón, F. J.; Errandonea, D.; Romero, A. H.; Garro, N.; Serrano, J.; Kuball, M. Lattice Dynamics of Wurtzite and Rocksalt AlN Under High Pressure: Effect of Compression on the Crystal Anisotropy of Wurtzite-Type Semiconductors. *Phys. Rev. B: Condens. Matter Mater. Phys.* **2008**, *77*, 205204.

(81) Manjón, F. J.; Syassen, K.; Lauck, R. Effect of Pressure on Phonon Modes in Wurtzite Zinc Oxide. *High Pressure Res.* **2002**, *22*, 299−304.

(82) Wang, Y. Q.; Lu, P. C.; Wu, J. J.; Liu, J.; Wang, X. C.; Zhao, J. Y.; Bi, W.; Alp, E. E.; Park, C. Y.; Popov, D.; et al. Phonon Density of States of Single-Crystal $SrFe_2As_2$ across the Collapse Phase Transition at High Pressure. *Phys. Rev. B: Condens. Matter Mater. Phys.* **2016**, *94*, 014516.

(83) Urbach, F. The Long-Wavelength Edge of Photographic Sensitivity and of the Electronic Absorption of Solids. *Phys. Rev.* **1953**, *92*, 1324.

(84) Tauc, J. Optical Properties and Electronic Structure of Amorphous Ge and Si. *Mater. Res. Bull.* **1968**, *3*, 37−46.

(85) Errandonea, D.; Muñoz, A.; Rodríguez-Hernández, P.; Proctor, J. E.; Sapiña, F.; Bettinelli, M. Theoretical and Experimental Study of the Crystal Structures, Lattice Vibrations, and Band Structures of Monazite-Type $PbCrO_4$, $PbSeO_4$, $SrCrO_4$, and $SrSeO_4$. *Inorg. Chem.* **2015**, *54* (15), 7524−7535.

(86) Ruiz-Fuertes, J.; Errandonea, D.; Manjón, F. J.; Martínez-García, D.; Segura, A.; Ursaki, V. V.; Tiginyanu, I. M. High-Pressure Effects on the Optical-Absorption Edge of $CdIn_2S_4CdIn_2S_4$, $MgIn_2S_4MgIn_2S_4$, and $MnIn_2S_4MnIn_2S_4$ Thiospinels. *J. Appl. Phys.* **2008**, *103*, 063710.

(87) Santamaria-Perez, D.; Ruiz-Fuertes, J. AB_2S_4 and AB_2Se_4 Compounds at High Pressures. In *Pressure-Induced Phase Transitions in AB_2X_4 Chalcogenide Compounds* Springer Verlag: 2014; pp 75−102.

(88) Manjón, F. J.; Gomis, O.; Rodríguez-Hernández, P.; Pérez-González, E.; Muñoz, A.; Errandonea, D.; Ruiz-Fuertes, J.; Segura, A.; Fuentes-Cabrera, M.; Tiginyanu, I. M.; et al. Nonlinear Pressure Dependence of the Direct Band Gap in Adamantine Ordered-Vacancy Compounds. *Phys. Rev. B: Condens. Matter Mater. Phys.* **2010**, *81*, 195201.

(89) Errandonea, D.; Muñoz, A.; Rodríguez-Hernández, P.; Gomis, O.; Achary, S. N.; Popescu, C.; Patwe, S. J.; Tyagi, A. K. High-Pressure Crystal Structure, Lattice Vibrations, and Band Structure of $BiSbO_4$. *Inorg. Chem.* **2016**, *55* (10), 4958−4969.

■ NOTE ADDED AFTER ASAP PUBLICATION

A partially corrected version of this paper was originally published on April 12, 2018. That version was removed and replaced with a fully corrected version of this paper on April 13, 2018.